Title:

Full title: Tuning intermediate filament mechanics by indirect and direct charge variations

Short title: Tuning intermediate filament mechanics

Authors: Anna V. Schepers[1], Charlotta Lorenz[1], and Sarah Köster[1]*

Affiliation: 1. Institute for X-Ray Physics, University of Goettingen,

Friedrich-Hund-Platz 1, 37077 Göttingen, Germany

*Corresponding author. Email: sarah.koester@phys.uni-goettingen.de

Abstract

The cytoskeleton is formed by three types of filamentous proteins – microtubules, actin filaments, and intermediate filaments (IFs) – and enables cells to withstand external and internal forces. Vimentin is the most abundant IF in humans and has remarkable mechanical properties, such as high extensibility and stability. It is, however, unclear to which extent these properties are influenced by the electrostatic environment. Here, we study the mechanical properties of single vimentin filaments by employing optical trapping combined with microfluidics. Force-strain curves, recorded at varying ion concentrations and pH values, reveal that the mechanical properties of single vimentin IFs are influenced by direct (pH) and indirect (ionic) charge variations. By combination with Monte Carlo simulations, we connect these altered mechanics to electrostatic interactions of subunits within the filaments. We thus find possible mechanisms that allow cells to locally tune their stiffness without remodelling the entire cytoskeleton.

One-Sentence-Summary: Adaptable force-strain behaviour of single cytoskeletal filaments in varying electrostatic conditions allow cells to tune their mechanical properties rapidly and locally.

MAINTEXT

Introduction

It is meanwhile well accepted that the mechanical properties of cells are, to a large extent, governed by the cytoskeleton, a stabilising, yet flexible framework, which is composed of microtubules, actin filaments, and intermediate filaments (IFs), together with motor proteins and crosslinkers. While microtubules and actin filaments are conserved in eukaryotic cell types, there are around 70 different genes encoding IFs in man that are expressed according to the cell's specific requirements *(1, 2)*.

Despite differences in their amino acid sequence, all cytoskeletal IF proteins share their secondary structure with a tripartite alpha-helical rod and disordered head and tail domains *(3, 4)*. During the hierarchical assembly, two monomers form a parallel coiled coil and these dimers organise into anti-parallel tetramers in a half-staggered arrangement. The tetramers assemble laterally to form unit length filaments (ULFs), which in turn elongate to filaments by end-to-end annealing *(3)*. The resulting biopolymer comprises a complex high-order arrangement of coiled coils *(3)*, which allows IFs to be extended up to at least 4.5-fold their initial length *(5–7)*. This enormous extensibility is in stark contrast to microtubules and F-actin *(8)*.

Vimentin is the IF typically expressed in mesenchymal cells *(2)* and up-regulated during the epithelial-to-mesenchymal transition in wound healing, early embryogenesis, and cancer metastasis *(9)*. In addition to being highly extensible *(7, 10, 11)* vimentin is flexible *(12–14)* and stable *(15)*. During stretching, three regimes are observed in the force-strain data *(7, 10, 11, 16, 17)*: an initial linear, elastic increase, a plateau of relatively constant force, and a subsequent stiffening regime. These regimes have been linked to structural changes in the protein *(16)*. The initial linear increase is described as elastic stretching of the filament consisting of the alpha-

2

46 helices, the plateau as the unfolding of alpha-helical structures, and the stiffening as the further

47 stretching of the unfolded structure.

48 A similar three-regime force-distance behaviour has been found for single coiled coils *(18, 19)*,

49 which are a common theme in protein structures. The overall structural stability of coiled coils

50 depends on the buffer conditions, however, the results are partially conflicting. Some studies

51 show an increased stability at low pH compared to neutral pH *(20, 21)*, whereas others find

52 higher stability in neutral pH conditions *(22, 23)*. It has been discussed that the response of

53 a coiled coil to altered pH conditions depends on the concentration of salt ions in the buffer

54 but also on the sequence of the peptide *(24)*. Molecular dynamics simulations of the isolated

55 vimentin coiled-coil dimer *(17)* agree qualitatively with experimental force-strain curves of

56 single coiled coils *(18, 19, 25)* and vimentin filaments *(7, 11)*. These results indicate that coiled

57 coils play a pivotal role in the force-strain response of mature IFs.

58 Here we address the open question of how strongly the variability of the mechanical response

59 observed for coiled coils in different measurement conditions is conserved in fully assembled

60 vimentin IFs. We study the response of mature vimentin IFs to tuning of the ionic conditions of

61 the buffer and to the internal charge distribution in the protein by adjusting the pH of the buffer,

62 and find that both factors strongly influence the mechanics of single vimentin IFs. Monte-Carlo

63 simulations enable us to link electrostatic interactions within the filament and modifications of

64 the free energy landscape of the unfolding reaction to the observed force-strain behaviour. The

65 possibility to tune filament mechanics fast and locally may have important implications within

66 living cells.

3

Results

Cations stiffen single vimentin IFs

To investigate the effect of the ionic environment on the mechanical behaviour of single vimentin filaments, we stretch the filaments after incubation in different buffers. For comparability, all filaments are assembled in standard assembly buffer (2 mM phosphate buffer (PB) with 100 mM KCl, pH 7.5, see Fig. 1a for a schematic representation of the hierarchical assembly pathway) before the stretching experiment. A single filament is then tethered to optically trapped beads and incubated in the respective measuring buffer for 30 s before stretching. A graphical protocol of the experiment is shown in Fig. 1b. Fig. 1c shows a typical resulting force-strain curve, where the strain is defined as $\varepsilon = (L - L_0)/L_0$ with the original filament length, L_0, measured at 5 pN force.

The mechanical response of single filaments to stretching shows a clear dependence on the experimental conditions, as shown in Fig. 2. All panels show average data and the individual curves are omitted here for clarity, but are shown in Supplementary Figs. S1 and S2. The three regimes that have been previously reported *(7, 10, 11, 16, 17)* are evident in the force-strain data recorded under standard assembly conditions as shown in Fig. 2a (100 mM KCl, see legend for colour code): The initial linear increase (I in Fig. 1c), the plateau (II) and the subsequent stiffening at high strains (III) can be clearly distinguished. Note that what we describe as "plateau" here does not necessarily have a slope of zero, but a considerably decreased slope compared to the rest of the curve. The curves recorded at high salt concentrations, *i.e.* $c(KCl) = 100$ mM or 150 mM and $c(MgCl_2) = 5$ mM or 10 mM, are consistent with this mechanical behaviour. In particular, the initial slopes, which describe the initial elasticity of the filament, agree well between these four salt conditions, as shown in detail by the solid circles in Fig. 3a. These values

4

90 are determined by fitting the initial slopes of the individual force-strain curves (Supplementary

91 Figs. S1 and S2).

92 When the filaments are incubated in low salt buffer (PB, pH 7.5), where tetramers are known

93 to be stable *(26)*, before stretching, the mechanics change significantly. Fig. 2a shows that

94 the complete curve is shifted to lower forces, the initial slope is lower and the plateau is less

95 pronounced. The decreased initial slope is indicative of a softer material. As a consequence of

96 this softening, the filament can be stretched to higher strains as compared to high salt buffers

97 before the maximum force of the optical trap is reached. The curve measured at 50 mM KCl

98 lies between the data for low salt buffer and the standard assembly buffer curve, as does the

99 maximum strain for this condition. Independent of the measuring conditions, the strain at which

100 the initial linear increase ends is at $\varepsilon_I = 0.14 \pm 0.04$ (see Fig. 2a), showing that the elastic

101 extensibilty of the filament is not affected by the salt ions. It is remarkable that the slope of the

102 plateau is constant for all buffers, as shown in Fig. 3a by the open circles.

103 Amino acids, the building blocks of proteins, may be either hydrophobic, polar or charged.

104 Ions in the buffer interact with those polar and charged amino acids that are accessible within a

105 supramolecular structure, thus mediating interactions within the assembled filament. Here, we

106 refer to such electrostatic interactions caused by ions in the buffer as *indirect* charge effects.

107 The similarity between the curves at $c(KCl) = 100$ mM or 150 mM and $c(MgCl_2) = 5$ mM or

108 10 mM indicates that predominantly the cations are causing the different behaviour and not the

109 Cl^- anions. In contrast, if it were mainly the Cl^- ions that caused the stiffening of the filaments,

110 we would expect the curve at $c(KCl) = 50$ mM to lie above both $MgCl_2$ curves since $c_{KCl}(Cl^-) >$

111 $c_{MgCl_2}(Cl^-)$ for all measured buffers.

112 The cations do not only stiffen but also stabilise the single filaments as shown in Fig. 3b by

5

the relative count of stable filaments (solid bars), metastable filaments (cross-hatched bars), and instable filaments (open bars). The stability is defined according to the maximum force reached during stretching, F_{max}. Filaments are sorted into the groups presented in Fig. 1c (instable: F_{max} < 100 pN, metastable: 100 pN < F_{max} < 650 pN, stable filaments: F_{max} > 650 pN or bead pulled out of trap). The fraction of stable filaments increases from 0.45 for the measurements in low salt buffer to 0.84 ± 0.06 (average and standard deviation from data at c(KCl) = 100 mM and 150 mM, and c(MgCl$_2$) = 5 mM and 10 mM) at higher salt concentrations. The cations additionally promote bundling (see Supplementary Fig. S3a). This observation agrees well with the reported behaviour of vimentin networks where – with increasing concentrations of multivalent ions – freely fluctuating networks collapse to dense aggregates *(27)*. Combined with these findings, our results show that the c(Mg^{2+}) dependent stiffening of vimentin networks, as previously suggested by rheology experiments *(13)*, is solely due to stronger interactions between filaments and no additional stiffening of single filaments in the network.

IF mechanics adapt to pH changes

Whereas the interactions of ions with the protein described in the previous section represent an indirect charge effect on the filament, we can also *directly* manipulate the charge of specific amino acids, *e.g.* by varying the pH of the buffer. To keep the two effects separate, at first, we use the curve recorded in the low salt buffer (2 mM PB, pH 7.5) as a starting point and do not add any additional salt ions. As the cytoplasmic pH in eukaryotic cells is reported to lie between 7.0 and 7.4 *(28)*, we lower the pH to 7.0. The resulting curves are shifted to higher forces and the plateau region is shorter compared to the low salt buffer at pH 7.5 (see Fig. 2b and Supplementary Fig. S2c,d). The stiffening effect is amplified at even lower pH as shown by data for pH 6.5 and pH 5.8. The curves recorded in these low pH conditions are remarkably

6

137 similar to each other and the filaments are considerably stiffer than in all previous measurement

138 conditions with the plateau almost disappearing. If we, in contrast, increase the pH from 7.5

139 to 8.5, the mechanics of the filament do not change. Thus, the adaption of the filament occurs

140 between pH 6.5 to 7.5 and it assumes an intermediate state at pH 7.0.

141 In line with the observations for varying salt concentrations reported above, the strain reached

142 with the initial, linear increase (ε_I =0.17±0.03) is not strongly influenced by the pH of the

143 measurement buffer. This result shows that the elastic extensibility of the filament is neither

144 strongly affected by direct nor by indirect charges. Additionally, the initial slope at low pH is

145 the same as for the standard assembly buffer or high salt concentrations (Fig. 3a,c), indicating

146 that low pH and high salt have a similar effect on the initial stiffness of the filament. The

147 decrease of the initial slope with increasing pH is plotted by solid circles in Fig. 3c and is evident

148 in the force-strain curves at low strains in Fig. 2b. In contrast to the cations, the pH clearly

149 affects the unfolding mechanism responsible for the plateau formation and the increased slope

150 of the plateau region at low pH suggests that the force needed for unfolding events increases

151 with decreasing pH. Because the onset of the stiffening moves to lower strains for low pH, the

152 strain range of the plateau becomes very short. Unlike for filaments in varying salt conditions

153 (Supplementary Fig. S4a), the ratio of the initial slope and slope of the plateau does not change

154 with the pH (Supplementary Fig. S4b).

155 Taken together, our force-strain data on vimentin IFs at different pH values show that the over-

156 all stiffness of the filament and the unfolding are altered considerably when the charge of a few

157 specific amino acids is varied. This assumption is further supported by the stability behaviour of

158 the filaments (see Fig. 3d). Here, the fraction of stable filaments, represented by solid bars, de-

159 creases with increasing pH, from 0.92 at pH 5.8 to 0.27 at pH 8.5, while the force-strain curves

160 do not change between pH 7.5 and 8.5 or between 5.8 and 6.5. A stabilisation or destabilisa-

7

161 tion therefore still continues even if the force-strain behaviour of the stable filaments are not

162 affected.

IF stiffening saturates at low pH

164 We observe an overall weaker stiffening by indirect (cationic) charge shifts compared to direct

165 (pH) charge shifts on single vimentin filaments. This phenomenon is especially prominent in

166 the plateau regions. To understand the interplay of the two effects, we compare two sets of

167 data recorded at different pH (7.5 and 5.8) without additional salt and with 100 mM KCl each.

168 The four average curves are shown in Fig. 2c. At pH 5.8, 100 mM KCl does not have a strong

169 effect, and the curves with and without additional salt are strikingly similar (purple), especially

170 when compared to the pronounced effect of 100 mM KCl at pH 7.5 (green). This observation

171 suggests that the stiffening is already saturated at low pH without salt and the ions only have

172 a negligible effect. To ensure that the saturation of the stiffening we observe at low pH is

173 constant on the time scales accessible here, we further investigate the temporal evolution of

174 the adaptation of the mechanics of the filament at low pH. The negligible difference between

175 curves (Supplementary Fig. S5) recorded at incubation times of 15 s, 30 s, and 60 s shows that

176 the additional interactions within the filaments have developed already after a few seconds.

Variations in the free energy landscapes influence filament mechanics

178 The observed filament softening in low salt buffer and stiffening at low pH raises the question

179 of how these mechanical properties are governed by molecular charge interactions within the

180 filament. To answer this question, we first regard the initial slope of the force-strain curves in

181 Fig. 2. The initial slope decreases when fewer monovalent cations are present and increases with

182 decreasing pH. In our 1D experimental setting, we can interpret the initial slope as a measure of

183 the filament stiffness, which for the sake of modelling we describe by the spring constant of the

8

184   filament, κ_f. We expect an increase with the number of monomers, N, per cross-section of the

185   filament *(29)*. We can, however, exclude the possibility of a reorganisation of mature filaments

186   *in vitro* by addition or loss of subunits as it only occurs on timescales of tens of minutes *(30)*

187   which is much slower than the time scales of our experiments. We can therefore safely assume

188   that the number of monomers is constant during our experiments. Instead, stiffening of the

189   filament may originate from an increase of the spring constant of an individual alpha-helix, κ_α,

190   as shown in the Monte-Carlo simulated force-strain curves in Fig. 4a. An increased stiffness

191   can furthermore be explained if we regard the filament as a bundle of protofilaments. If these

192   protofilaments are fully coupled to each other, the persistence length of the bundle increases as

193   N^2 instead of linearly in N in the uncoupled case *(29)*. An increase in coupling strength and

194   thus an increased initial slope may be caused by higher salt concentration or lower pH and is

195   thus in line with our experimental results. It should be noted, however, that we do not include

196   this effect in our simulations. Instead, we simulate 'subunit coupling', see Fig. 4b, that describes

197   the size of fully coupled lateral subunits into which the monomers are organised *(31)*. Thus,

198   in higher order subunits, more elements have to unfold simultaneously to achieve the length

199   change, ΔL, of the filament. This effect already plays a role for the initial stretching and leads

200   to a slightly increased slope (see inset of Fig. 4b).

201   The origin of intra-filament coupling is found in the structure of vimentin. Each vimentin

202   monomer has an excess of -19 e negative charges. A representation of the charge distribution

203   in the vimentin monomer is shown in Fig. 5a. The excess negative charges are mostly found in

204   coil 1B, coil 2 and the tail. As most polar and charged amino acids are not buried within the

205   alpha-helix *(32)*, the excess negative charges of neighbouring monomers within the filaments

206   are likely to be in close proximity. The resulting repulsion presumably destabilises the filament

207   structure. The decreased initial slope and reduced stability we observe in low salt conditions

9

208 therefore indicates that cations screen or – in case of multivalent ions – cross-bridge these

209 repulsions. This is supported by the fact that vimentin is known to assemble in the presence of

210 a sufficiently high concentration of cations and to disassemble in low salt buffer *(26)*.

211 In contrast to the ion mediated, indirect, electrostatic effect, a pH change directly influences the

212 charge pattern of the protein sequence. To be specific, in the pH range used here, we switch his-

213 tidines from being uncharged to positively charged in an acidic environment. In vimentin there

214 are six histidines at various positions, indicated by the arrows in Fig. 5a. These additional pos-

215 itive charges increase the number of possible electrostatic interaction sites between monomers

216 in the filament (Fig. 5b), and therefore in our case decrease the repulsion, increase attraction,

217 and promote coupling in the filament, similar to added ions.

218 Whereas the change of the initial slope is well explained by variations of κ_α, other experiment-

219 ally observed changes in the force-strain curves, such as the plateau slope and length are not

220 reproduced by this variation. To be able to compare the mechanisms that affect the plateau, we

221 first examine the unfolding reaction that leads to the plateau formation. The force level of the

222 plateau F_{plateau} (Fig. S6), the force reached at strain $\varepsilon_{\text{I}}1$, is a measure of the energy necessary

223 for unfolding. Fig. 4c shows a schematic and simplified energy landscape for the transition

224 from the alpha- to the unfolded state (green). The energy barrier E_A between the two states is

225 indicated in Fig. 4d. The optical trap is approximated by a harmonic potential (dashed line). By

226 applying a force (Fig. 4d), the harmonic potential is moved to the right, thereby decreasing the

227 energy barrier in the total potential (blue) and the unfolded state becomes more probable.

228 The simulated force-strain curves in Fig. 4b reveal a strong dependence of F_{plateau} on the subunit

229 size. By choosing a small subunit size such as $N_{sub} = 4$ we are able to reproduce the observed

230 decrease of F_{plateau} in low salt buffer. At low pH, F_{plateau} is even higher than in high salt buffer.

10

231 Thus, E_A is apparently even further increased at low pH. This behaviour may be explained by

232 an increased free energy difference, ΔG, between the alpha- and unfolded state (purple curve

233 in Fig. 4h as compared to green curve in Fig. 4d), thus rendering the transition from the alpha-

234 to the unfolded state less probable at the same applied force (Fig. 4g,h), effectively increasing

235 F_{plateau}. Fig. 4e shows how ΔG influences the force-strain curve.

236 In addition to an increased F_{plateau}, we also observe a shortening of the plateau at low pH

237 (Fig. 2b). The length of the plateau, $\varepsilon_{\text{II}} - \varepsilon_{\text{I}}$, depends on the number of unfolding events

238 and the length increase during unfolding, ΔL. Here, by the 'number of unfolding events' we

239 summarise (i) fully unfolded ULFs and (ii) partially unfolded ULFs, as each of them consists

240 of 32 monomers with three coils each, which can unfold fully or in parts. As ε_{I} is relatively

241 constant in all measuring conditions, ε_{II} is a measure for the length of the plateau. Fig. 4f

242 demonstrates how a decrease of ΔL shortens the plateau.

243 Earlier interpretations of the plateau being a transition from the alpha-helices to beta-sheets

244 would allow for an elongation to strain 0.77 *(7, 17)* in the plateau. This value agrees with ε_{II} at

245 high salt concentrations, but is exceeded at low salt conditions and not reached at low pH values

246 (Fig. 2). Recent results indicate that the unfolding is in fact not a two-state process but that

247 alpha-helices first unfold to a random coil structure *(33)*. These random coils could be either

248 longer or shorter than the beta-sheet conformation and thereby explain the variations in ΔL.

249 The remarkably short plateaus we observe at low pH indicate a strong influence of the pH on

250 ΔL. From the simulation in Fig. 4f we learn that decreasing ΔL furthermore increases the slope

251 of the plateau, which agrees well with the increase of the slope we observe at low pH (Fig. 3c).

252 The additional positive charges located at the sites of the histidines might act as crosslinkers in

253 the filament, 'locking' the monomers in place and thereby decreasing ΔL.

11

254 Combining the simulations and the experimental results, we are now able to explain the ob-

255 served increase of the initial slope, shortening of the plateau, shift to higher forces F_{plateau} at

256 low pH or high salt conditions by increased subunit coupling and decreased ΔL. Additionally,

257 for the low pH conditions, a more pronounced ΔG comes into play, whereas for high salt, κ_α

258 is increased. The slope of the plateau can be modelled by a decrease of the subunit size or of

259 ΔL. As we observe no change of the slope of the plateau throughout all salt conditions at pH

260 7.5, these effects seem to be balance out during the plateau formation.

Discussion

262 Previous studies of the stability of single coiled coils at varying pH and ionic strength showed

263 partially conflicting results *(20, 22, 24)*. These opposing observations can be understood in

264 the light of different primary sequences that lead to coiled coils of varying stability, based on

265 the length of the coils *(19)*, the hydrophobic packing or helix propensity, *i.e.* how prone an

266 amino acid is to form alpha-helical structures *(25)*, and electrostatic interactions in the coil

267 *(20, 22, 24)*. The effect of the electrostatic environment we report here is valid for vimentin

268 but might be considerably weaker or stronger for other types of IFs. As the charge patterns in

269 different types of IFs vary, the extent of the effect of salt ions scales according to the strength

270 of the repulsion between subunits in the different IFs. For example, similar IFs, such as desmin

271 and glial fibrillary acidic protein (GFAP) have an excess charge of -15 e and -13 e, respectively.

272 We therefore expect the effect of ions to be weaker in these filaments *(1)*. We further expect the

273 effect of pH changes in the physiologically relevant range to scale with the number of histidines

274 per monomer. Whereas vimentin and desmin have six histidines ($N_H = 6$), GFAP ($N_H = 8$)

275 contains more potential additional interaction sites at low pH *(1)*. The effect in GFAP may

276 therefore be even stronger than observed here for vimentin.

277 As the cytoplasmic pH typically lies between 7.0-7.5 *(34)*, the mechanical properties of vi-

278 mentin are susceptible to pH changes in this range. Thus, cells are equipped with a "tool" to

279 rapidly and locally tune their stiffness without remodelling the whole cytoskeleton. However,

280 it remains unclear, how relevant the adaptability of the IF mechanics is in living cells. One

281 intriguing phenomenon, where considerable pH changes and the up-regulation of vimentin in

282 epithelial cells coincide, is wound healing. In epithelial wounds, mesenchymal cells expressing

283 vimentin promote healing of the skin. During the restoration of the tissue, these cells might

284 be exposed to pH milieus reaching from the healthy skin pH (4.0-6.0) to the body's internal

285 pH (7.0-7.4) *(28, 35)*. Vimentin is not only up-regulated in the cells but also excreted into the

286 extracellular space *(36)*. The result of our studies suggest that the mechanical changes vimentin

287 undergoes in this pH range are considerable and might play a role within cells as well as the

288 extracellular space during skin repair.

289 To conclude, we directly relate the mechanical response of single vimentin filaments to stretch-

290 ing in different buffer conditions to variations in the molecular electrostatic interactions in the

291 filament. Our results show that the strong response to the electrostatic environment reported for

292 coiled coils is preserved in mature vimentin filaments. A likely interpretation is that salt ions

293 in the buffer screen or bridge electrostatic repulsion in the hierarchical structure and thereby

294 stabilise the filaments. Additional positive charges in the amino acid sequence caused by a

295 lowered pH stabilise and stiffen vimentin filaments as well. Thus, our results indicate that the

296 mechanical role of IFs in cells can adapt to local pH and ion concentrations. Both effects, salt

297 and pH, may allow cells to locally tune their stiffness without having to rebuild the entire cyto-

298 skeleton and thereby adapt their mechanics to varying requirements. In this context, we show

299 that stiffening of vimentin networks that was previously reported upon the addition of Mg^{2+}

300 relies on increased inter-filament interactions and does not originate form stiffening of single

13

301 filaments. Thus, by ensuring a relatively constant stiffness, extensibility, force-strain behaviour,

302 and stability of the filaments at physiological potassium concentrations and in conditions that

303 are known to affect the bundling behaviour of vimentin, we suggest that network mechanics can

304 be tuned independent of the single filament properties.

14

Materials and methods

Experimental Design

The experiments were performed using a setup that combines optical traps, confocal microscopy and microfluidics (C-Trap, Lumicks, Netherlands). A four-inlet glass microfluidic flow cell enabled easy change of buffer during the experiment as the sub-channels in the flow cell were separated by laminar flow. The syringes feeding the microfluidic flow cell were driven by air pressure. Solutions were injected into the four channels as follows and as shown in Supplementary Fig. S8a: 1: beads in measuring buffer, 2: measuring buffer, 3: assembly buffer, 4: vimentin in assembly buffer. Figure 1b shows a simplified sketch, excluding channel 2 that is used for calibration of the traps. For the optical trap measurements, the filaments were diluted 150-fold in assembly buffer. Maleimide-functionalised polystyrene beads (Kisker Biotech, Steinfurt, Germany) *(11, 37)* were diluted in measuring buffer. The optical trap was calibrated by analysis of the power spectral density of the thermal fluctuations of the trapped beads. Filaments were tethered to trapped beads in assembly buffer in flow. The flow was then stopped, the beads with the tethered filament were moved to the measuring buffer and the filaments incubated for 30 seconds without flow. The filaments were stretched at a loading rate of 0.21 ± 0.05 μm/s. For each condition, force-strain curves of at least seven single, stable filaments were recorded. As measuring buffers we used 2 mM PB at varying pH (5.8 - 8.5) and concentrations of KCl (0, 50, 100, 150 mM) or $MgCl_2$ (0, 5, 10 mM) (Carl Roth, Germany). The concentrations and pH conditions given are the buffers that were injected into the microfluidic chip. Because the flow was stopped during incubation and stretching of the filaments, diffusion of the cations between the assembly and measuring buffers, and the assimilation of the pH have to be considered. This means that the conditions in proximity to the filament during the measurement were slightly different to the injected buffer. The temporal development of

15

329 the salt concentrations and the pH at the measurement position was simulated and is described

330 below.

Protein preparation

332 Human vimentin (mutant C328N with three additional amino acids, GGC, at the C-terminus)

333 was recombinantly expressed and purified as previously described *(11)*. The protein was la-

334 belled with ATTO647N maleimide (ATTO-Tec, Germany) *(30, 38)*. Reconstitution and as-

335 sembly was performed as previously reported *(11)*. In brief, unlabelled and labelled monomers

336 were mixed (4% labelling ratio) and reconstituted at room temperature by dialysis into 2 mM

337 phosphate buffer (PB, Carl Roth, Germany) at pH 7.5, decreasing the Urea (Carl Roth, Ger-

338 many) concentration every 30 min in steps of 6, 4, 2, 1, 0 M Urea and an subsequent overnight

339 dialysis step at 8-10 °C. Filaments were assembled by dialysis into assembly buffer (2 mM PB

340 with 100 mM KCl (Carl Roth, Germany) at pH 7.5) at 36 °C for 16 h at a protein concentration

341 of 0.2 g/L.

Data analysis

343 From confocal videos of the filament stretching and the force-strain behaviour, bundles were

344 identified and the force-strain curves of the bundles excluded from further analysis.

Calculation of single force-strain curves: For each filament, the initial length, L_0, was de-

346 termined and used for the calculation of the strain: $\varepsilon = (L - L_0)/L_0$. To obtain L_0, the raw

347 force-distance curve was smoothed with a moving average with a window width of 10 data

348 points to account for fluctuations of the trap. The initial length was set as the length at the last

349 data point before the smoothed curve reached 5 pN.

Analysis of the filament stability: Data curves were sorted according to the maximum force

351 reached during stretching, F_{max}, into the groups presented in Fig. 1c (instable: $F_{max} < 100$ pN,

16

metastable: 100 pN $< F_{max} < 650$ pN, stable filaments: $F_{max} > 650$ pN or bead pulled out of trap). For stable and metastable filaments, the force-strain curves were plotted.

Calculation of average force-strain curves: For each condition, the average maximum strain of all stable filaments was calculated. Each stable force-strain curve was scaled to the average maximum strain, interpolated to 200 values, and the forces were averaged. Metastable filaments were weighted according to the total number of stable and metastable curves and projected onto the average curve up to their yield-strain *(31)*.

Analysis of the slope of the plateaus: The plateau of each single force-strain curve was analysed for all stable filaments as they show a complete plateau. A typical analysis for one single force-strain curve is shown in Supplementary Fig. S7. The point of maximum strain, $\varepsilon_{\max}$, of each curve was used to find the mid data point, $\varepsilon_{\mathrm{mid}}$, of the curve (yellow in Supplementary Fig. S7a). The data points with relatively constant slope were determined. To do so, the differential of each single force-strain curve was calculated. To account for changes in length of the curve and noise of the data, each differential force-strain curve was then smoothed using a moving average with the width of $\frac{1}{20}$ of the number of data points in the curve before $\varepsilon_{\max}$. The values $\frac{dF}{d\varepsilon}$ at the 10 data points before and after $\varepsilon_{\mathrm{mid}}$ were averaged to find $\frac{dF}{d\varepsilon}(\varepsilon_{\mathrm{mid}})$. Next, the first maximum of $\frac{dF}{d\varepsilon}$, position A, was calculated (marked in Supplementary Fig. S7a). The first and last data point to fulfil $\frac{dF}{d\varepsilon} < \varepsilon_{\mathrm{mid}} + 0.35\cdot\left(\frac{dF}{d\varepsilon}(\mathrm{A})\text{-}\frac{dF}{d\varepsilon}(\varepsilon_{\mathrm{mid}})\right)$ were termed ε_{I} (red, solid) and $\varepsilon_{\mathrm{II}}$ (blue, solid), respectively. To ensure that the transition regions between I, II and III were not included in the analysis of the slope of the plateau, a linear regression (green line) of the force-strain curve was calculated for the centre 80% of the length of the plateau (between the open red and blue circles). The mean slope and standard deviation were calculated for each measuring condition.

17

Analysis of the force of the plateaus: For the analysis of F_{plateau}, ε_{I} determined from the average force-strain curve for each condition was used. The force at ε_{I} for each single force-strain curve was determined and the mean value and standard deviation were calculated.

Determination of the end points of the elastic and plateau regions: For the determination of the slope of the plateau, the regression was calculated over a large region of the force-strain curve. This approach compensated for noise in the data. However, the noise limits the accurate determination of ε_{I} and ε_{II}. Therefore, for the analysis of ε_{I} and ε_{II} for each condition, the average force-strain curves were used as shown in Fig. 2. The average curves were treated in the same way described above for the single force-strain curves. The only difference was that here the $\frac{dF}{d\varepsilon}$ curves were smoothed with a moving average of 15 data points.

Analysis of the initial slope of the force-strain curves: The initial slope was determined for strains from 0.02 to 0.1 or to a force of 100 pN, whichever occurred earlier.

Flow simulations

A simplified microfluidic chip design (Supplementary Fig. S8a) was used for finite element method (FEM) simulations with COMSOL Multiphysics 5.3 (COMSOL GmbH, Göttingen, Germany). Flow and diffusion were simulated for an average velocity of 0.001 m/s laminar inflow for each inlet for water with K^+ ($D_{\text{K}} = 1.67\ 10^{-9}$ m^2/s) *(39)* or Mg^{2+} ($D_{\text{Mg}} = 0.594\ 10^{-9}$ m^2/s) ions *(39)*. For the pH, the concentration of hydrogen ions $c(H^+)$ was calculated as $c(H^+) = 10^{\text{-pH}}$ and the diffusion of H^+ was estimated by ($D_H = 8.17\ 10^{-9}$ m^2/s) *(39)*. First, the equilibrium ion distribution in the chip was simulated under flow. Taking this as a starting condition, a second simulation was calculated without flow, only allowing diffusion. The change of the concentrations of the cations and H^+ ions was simulated at the position of the force-strain measurement (Supplementary Fig. S8a, red mark) for a duration of 5 min. The

18

398 equilibrium pH is reached within the first minute and then stays relatively constant over time

399 and in the flow cell. This resulting equilibrium pH was clearly distinguishable for the different

400 measuring buffers. The change of cation concentrations (Mg^{2+} from the measuring buffer, K^+

401 from the adjacent assembly buffer) is shown in Supplementary Fig. S8b for the example of the

402 10 mM $MgCl_2$ measuring buffer.

Force-strain Monte-Carlo simulations

404 A vimentin filament was mechanically modelled as previously described *(11, 31)*. The force-

405 strain behaviour of the modelled filament was determined by a Monte-Carlo simulation written

406 in MatLab *(31)*. The simulation was run with one varied parameter while keeping the others

407 constant as shown in Fig. 4a,b,e,f. The default parameters were the alpha-helical spring constant

408 ($\kappa_\alpha = 5.5$), the number of monomers in a subunit ($N_{sub} = 32$), the free energy difference

409 between the alpha-state and unfolded state ($\Delta G = 2$) and the length by which an alpha-helix

410 can extend upon unfolding $\Delta L = 1$.

19

Supplementary Materials

Fig. S1. Force-strain curves for each salt condition measured.

Fig. S2. Force-strain curves for each pH condition measured.

Fig. S3. Relative count of single filaments and bundles for each condition.

Fig. S4. Ratio of the initial slope and the slope of the plateau for each measuring condition.

Fig. S5. Force-strain curves for filaments stretched in phosphate buffer (PB), pH 5.8 with varying incubation times.

Fig. S6. Plateau force of the force-strain curves.

Fig. S7. Analysis of the slope of the plateau for one single force-strain curve.

Fig. S8. Results of FEM simulations.

References

[1] I. Szeverenyi, A. J. Cassidy, C. W. Chung, B. T. Lee, J. E. Common, S. C. Ogg, H. Chen, S. Y. Sim, W. L. Goh, K. W. Ng, J. A. Simpson, L. L. Chee, G. H. Eng, B. Li, D. P. Lunny, D. Chuon, A. Venkatesh, K. H. Khoo, W. I. McLean, Y. P. Lim, and E. B. Lane, "The human intermediate filament database: comprehensive information on a gene family involved in many human diseases," *Hum. Mutat.*, vol. 29, no. 3, pp. 351–360, 2008.

[2] J. E. Eriksson, T. Dechat, B. Grin, B. Helfand, M. Mendez, H.-M. Pallari, and R. D. Goldman, "Introducing intermediate filaments : from discovery to disease," *J. Clin. Invest.*, vol. 119, pp. 1763–1771, 2009.

[3] H. Herrmann, M. Häner, M. Brettel, S. A. Müller, K. N. Goldie, B. Fedtke, A. Lustig, W. W. Franke, and U. Aebi, "Structure and assembly properties of the intermediate fila-

20

ment protein vimentin: The role of its head, rod and tail domains," *J. Mol. Biol.*, vol. 264, pp. 933–953, 1996.

[4] A. A. Chernyatina, D. Guzenko, and S. V. Strelkov, "Intermediate filament structure: The bottom-up approach," *Curr.Opin. Cell Biol.*, vol. 32, pp. 65–72, 2015.

[5] L. Kreplak, H. Bär, J. F. Leterrier, H. Herrmann, and U. Aebi, "Exploring the mechanical behavior of single intermediate filaments," *J. Mol. Biol.*, vol. 354, pp. 569–577, 2005.

[6] L. Kreplak, H. Herrmann, and U. Aebi, "Tensile properties of single desmin intermediate filaments," *Biophys. J.*, vol. 94, pp. 2790–2799, 2008.

[7] J. Block, H. Witt, A. Candelli, E. J. G. Peterman, G. J. L. Wuite, A. Janshoff, and S. Köster, "Nonlinear loading-rate-dependent force response of individual vimentin intermediate filaments to applied strain," *Phys. Rev. Lett.*, vol. 118, p. 048101, 2017.

[8] P. A. Janmey, U. Euteneuer, P. Traub, and M. Schliwa, "Viscoelastic properties of vimentin compared with other filamentous biopolymer networks," *J. Cell Biol.*, vol. 113, no. 1, pp. 155–160, 1991.

[9] M. Zeisberg and E. G. Neilson, "Biomarkers for epithelial-mesenchymal transitions," *J. Clin. Invest.*, vol. 119, no. 6, pp. 1429–1437, 2009.

[10] N. Pinto, F.-C. Yang, A. Negishi, M. C. Rheinstä, T. E. Gillis, and D. S. Fudge, "Self-assembly enhances the strength of fibers made from vimentin intermediate filament proteins," *Biomacromolecules*, vol. 15, pp. 574–581, 2014.

[11] J. Block, H. Witt, A. Candelli, J. C. Danes, E. J. Peterman, G. J. Wuite, A. Janshoff, and

21

452   S. Köster, "Viscoelastic properties of vimentin originate from nonequilibrium conforma-
453   tional changes," *Sci. Adv.*, vol. 4, p. eaat1161, 2018.

454 [12] N. Mücke, L. Kreplak, R. Kirmse, T. Wedig, H. Herrmann, U. Aebi, and J. Langowski,
455   "Assessing the flexibility of intermediate filaments by atomic force microscopy," *J. Mol.*
456   *Biol.*, vol. 335, pp. 1241–1250, 2004.

457 [13] Y. C. Lin, C. P. Broedersz, A. C. Rowat, T. Wedig, H. Herrmann, F. C. MacKintosh, and
458   D. A. Weitz, "Divalent cations crosslink vimentin intermediate filament tail domains to
459   regulate network mechanics," *J. Mol. Biol.*, vol. 399, pp. 637–644, 2010.

460 [14] B. Nöding and S. Köster, "Intermediate filaments in small configuration spaces," *Phys.*
461   *Rev. Lett.*, vol. 108, p. 088101, 2012.

462 [15] C. Guzmán, S. Jeney, L. Kreplak, S. Kasas, A. J. Kulik, U. Aebi, and L. Forró, "Explor-
463   ing the mechanical properties of single vimentin intermediate filaments by atomic force
464   microscopy," *J. Mol. Biol.*, vol. 360, pp. 623–630, 2006.

465 [16] T. Ackbarow and M. J. Buehler, "Superelasticity, energy dissipation and strain harden-
466   ing of vimentin coiled-coil intermediate filaments: Atomistic and continuum studies," *J.*
467   *Mater. Sci.*, vol. 42, pp. 8771–8787, 2007.

468 [17] Z. Qin, L. Kreplak, and M. J. Buehler, "Hierarchical structure controls nanomechanical
469   properties of vimentin intermediate filaments," *PLoS ONE*, vol. 4, no. 10, p. e7249, 2009.

470 [18] D. D. Root, V. K. Yadavalli, J. G. Forbes, and K. Wang, "Coiled-coil nanomechanics and
471   uncoiling and unfolding of the superhelix and α-helices of myosin," *Biophys. J.*, vol. 90,
472   pp. 2852–2866, 2006.

[19] M. Goktas, C. Luo, R. M. A. Sullan, A. E. Bergues-Pupo, R. Lipowsky, A. Vila Verde, and K. G. Blank, "Molecular mechanics of coiled coils loaded in the shear geometry," *Chem. Sci.*, vol. 9, pp. 4610–4621, 2018.

[20] K. Dutta, A. Alexandrov, H. Huang, and S. M. Pascal, "pH-induced folding of an apoptotic coiled coil," *Protein Sci.*, vol. 10, pp. 2531–2540, 2001.

[21] M. M. Stevens, S. Allen, J. K. Sakata, M. C. Davies, C. J. Roberts, S. J. Tendler, D. A. Tirrell, and P. M. Williams, "pH-Dependent behavior of surface-immobilized artificial leucine zipper proteins," *Langmuir*, vol. 20, no. 18, pp. 7747–7752, 2004.

[22] K. Pagel, S. C. Wagner, K. Samedov, H. Von Berlepsch, C. Böttcher, and B. Koksch, "Random coils, β-sheet ribbons, and α-helical fibers: one peptide adopting three different secondary structures at will," *J. Am. Chem. Soc.*, vol. 128, pp. 2196–2197, 2006.

[23] R. M. Reja, M. Khan, S. K. Singh, R. Misra, A. Shiras, and H. N. Gopi, "pH sensitive coiled coils: A strategy for enhanced liposomal drug delivery," *Nanoscale*, vol. 8, pp. 5139–5145, 2016.

[24] Y. Yu, O. D. Monera, R. S. Hodges, and P. L. Privalov, "Ion pairs significantly stabilize coiled-coils in the absence of electrolyte," *J. Mol. Biol.*, vol. 255, pp. 367–372, 1996.

[25] P. López-García, M. Goktas, A. E. Bergues-Pupo, B. Koksch, D. Varón Silva, and K. G. Blank, "Structural determinants of coiled coil mechanics," *Phys. Chem. Chem.Phys.*, vol. 21, pp. 9145–9149, 2019.

[26] H. Herrmann and U. Aebi, "Intermediate filament assembly: fibrillogenesis is driven by decisive dimer-dimer interactions," *Curr. Opin. Struc. Biol.*, vol. 8, pp. 177–185, 1998.

[27] C. Dammann and S. Köster, "Dynamics of counterion-induced attraction between vimentin filaments followed in microfluidic drops," *Lab Chip*, vol. 14, pp. 2681–2687, 2014.

[28] G. R. Bright, G. W. Fisher, J. Rogowska, and D. L. Taylor, "Fluorescence ratio imaging microscopy: temporal and spatial measurements of cytoplasmic pH," *J. Cell Biol.*, vol. 104, pp. 1019–1033, 1987.

[29] J. F. Nolting, W. Möbius, and S. Köster, "Mechanics of individual keratin bundles in living cells," *Biophys. J.*, vol. 107, no. 11, pp. 2693–2699, 2014.

[30] B. Nöding, H. Herrmann, and S. Köster, "Direct observation of subunit exchange along mature vimentin intermediate filaments," *Biophys. J.*, vol. 107, pp. 2923–2931, 2014.

[31] C. Lorenz, J. Forsting, A. V. Schepers, J. Kraxner, S. Bauch, H. Witt, S. Klumpp, and S. Köster, "Lateral subunit coupling determines intermediate filament mechanics," *bioRxiv*, p. doi10.1101/676197, 2019.

[32] J. M. Mason and K. M. Arndt, "Coiled coil domains: stability, specificity, and biological implications," *ChemBioChem*, vol. 5, pp. 170–176, 2004.

[33] J. Forsting, J. Kraxner, H. Witt, A. Janshoff, and S. Köster, "Vimentin intermediate filaments undergo irreversible conformational changes during cyclic loading," *bioRxiv*, p. doi10.1101/673673, 2019.

[34] W. H. Moolenaar, L. G. J. Tertoolen, and S. W. De Laat, "The regulation of cytoplasmic pH in human fibroblasts," *J. Biol. Chem.*, vol. 259, no. 12, pp. 7563–7569, 1984.

[35] L. A. Schneider, A. Korber, S. Grabbe, and J. Dissemond, "Influence of pH on wound-

healing: A new perspective for wound-therapy?," *Arch. Dermatol. Res.*, vol. 298, pp. 413–420, 2007.

[36] J. L. Walker, B. M. Bleaken, A. R. Romisher, A. A. Alnwibit, and A. S. Menko, "In wound repair vimentin mediates the transition of mesenchymal leader cells to a myofibroblast phenotype," *Mol. Biol. Cell*, vol. 29, no. 13, pp. 1555–1570, 2018.

[37] R. Janissen, B. A. Berghuis, D. Dulin, M. Wink, T. Van Laar, and N. H. Dekker, "Invincible DNA tethers: Covalent DNA anchoring for enhanced temporal and force stability in magnetic tweezers experiments," *Nucleic Acids Res.*, vol. 42, no. 18, p. e137, 2014.

[38] S. Winheim, A. R. Hieb, M. Silbermann, E.-M. Surmann, T. Wedig, H. Herrmann, J. Langowski, and N. Mücke, "Deconstructing the late phase of vimentin assembly by total internal reflection fluorescence microscopy (TIRFM)," *PLoS ONE*, vol. 6, no. 4, p. e19202, 2011.

[39] Y.-H. Li and S. Gregory, "Diffusion of ions in sea water and in deep-sea sediments," *Geochim. Cosmochim. Ac.*, vol. 38, pp. 703–714, 1974.

Author contributions: SK conceived and supervised the project. AVS performed the experiments and the data analysis. CL developed the method for force-strain data averaging, implemented the model and performed the simulations. SK and AVS wrote the manuscript. All authors read and commented on the manuscript.

Competing interests: The authors declare no conflict of interest.

**Data Availability:** All data that support the findings of this study are presented in the main text and Supporting Information. Upon reasonable request, raw data will be made available by the corresponding author.
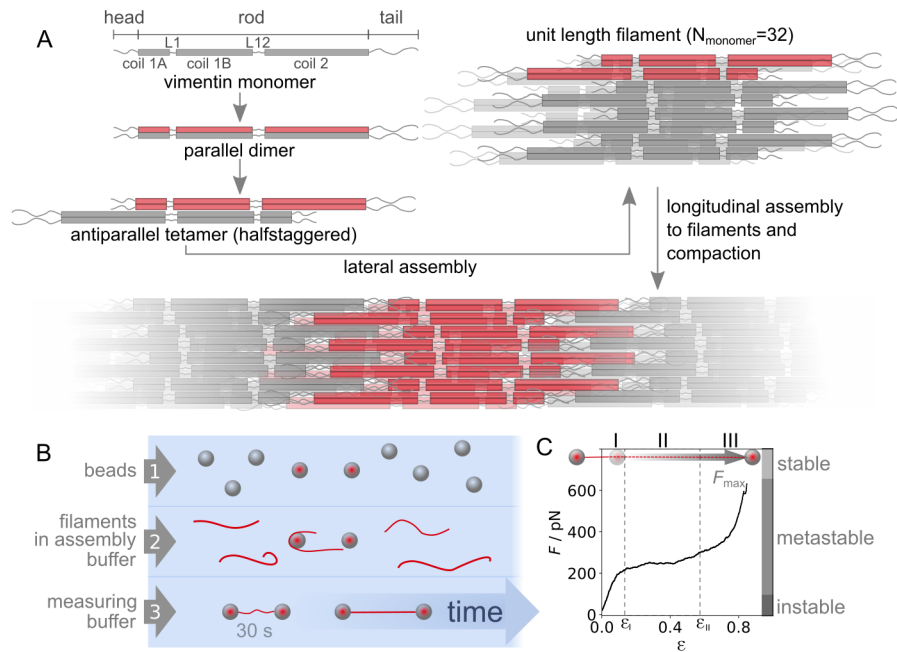
Fig. 1: Stretching experiments on fully assembled vimentin filaments. **(A)** Schematic of the hierarchical assembly of vimentin monomers into filaments. In each step, the respective precursor subunit is highlighted in red. **(B)** Measurement protocol of the optical trap experiment in microfluidic flow channels: Two beads are captured and calibrated (1), a single filament is covalently attached to both beads (2) and stretched after a 30 s incubation period in the measuring buffer (3). **(C)** Typical force-strain curve for a vimentin filament showing the elastic (I), plateau (II) and stiffening (III) regime. The strain at the transition of region I to II is ε_{I}, from II to III it is $\varepsilon_{\mathrm{II}}$. The force ranges for classifying the filaments according to their stability are indicated on the right.

27
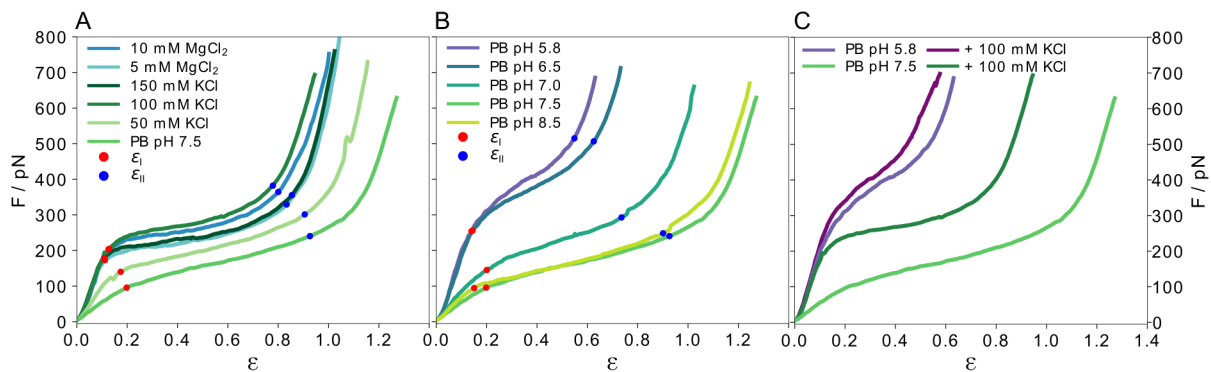


Fig. 2: Force-strain behaviour of single vimentin filaments. All curves shown are averages of the individual measurements shown in Supplementary Figs. S1 and S2. The strain values at the end of the initial linear regime ε_I (red) and the plateau regime ε_II (blue) for all average curves are indicated. **(A)** Effect of indirect charge shifts caused by salt ions in the measurement buffer. **(B)** Effect of direct charge shifts by varying pH conditions. While ε_I is similar in all measurements, ε_II increases for lower c(KCl) and for increasing pH. **(C)** Comparison of the effect of an addition of 100 mM K$^+$ ions at pH 7.5 and 5.8.
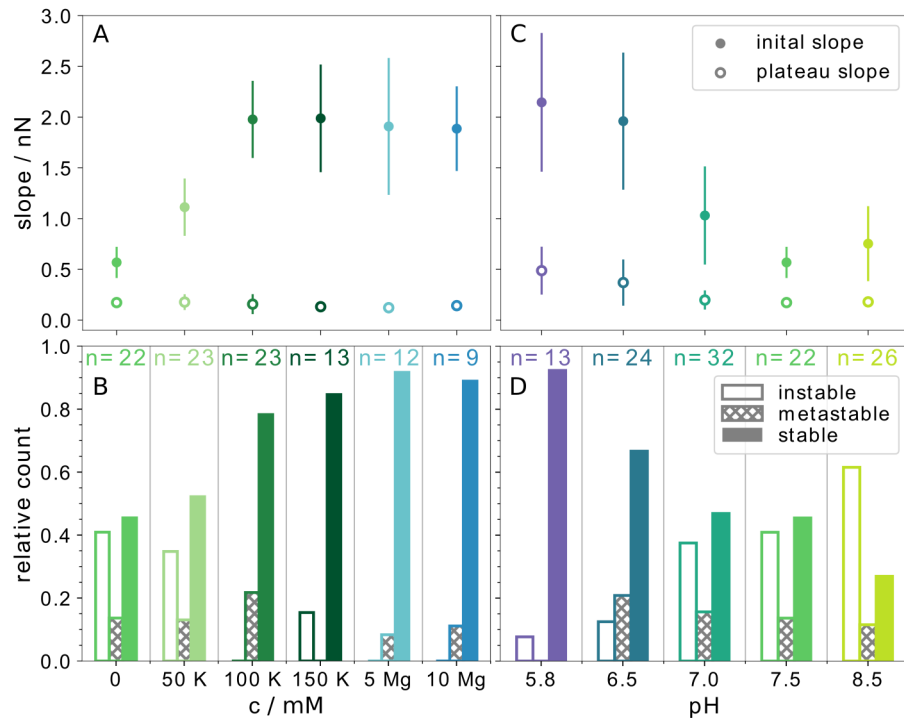
Fig. 3: Mechanical properties of single vimentin filaments. (A),(C) Analysis of the initial slopes (solid circles) and slopes of the plateau regions (open circles) of all metastable and stable filaments. The error bars indicate the standard deviation. **(B),(D)** The stability of the measured filaments is presented as fractions of instable, metastable and stable filaments.
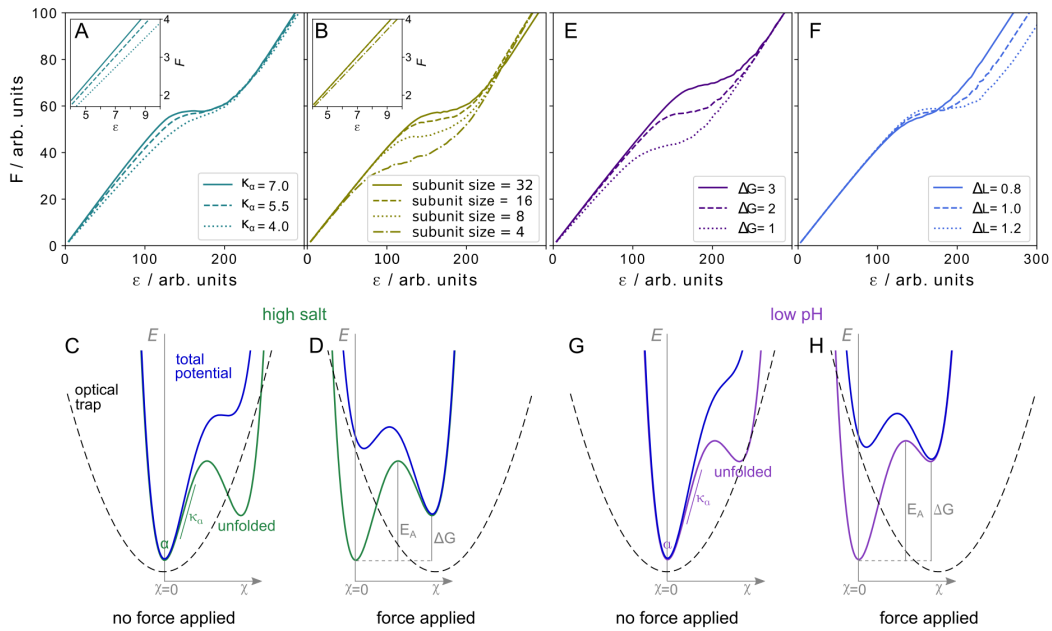
Fig. 4: Monte-Carlo simulations of force-strain curves and schematics of energy landscapes. **(A)** An increased κ_α causes an increase of the initial slope. **(B)** A stronger coupling into larger subunits moves the plateau to higher forces, decreases the slope of the plateau and weakly influences the initial slope. The insets in a and b show the initial slope for each parameter set. **(C)** Energy landscape E plotted against the reaction coordinate χ with minima for the alpha- and unfolded state at high salt conditions (green) within the harmonic potential corresponding to the optical trap (dashed line). The resulting total potential is shown in blue. Without applied load, the alpha-state is stable. **(D)** By moving the optical trap, and thereby the harmonic potential, the energy barrier is reduced and the unfolded state becomes more probable. **(E)** A higher free energy difference ΔG between the alpha- and unfolded state increases F_{plateau} without affecting the slope of the plateau. **(F)** Increasing the length of the unfolded monomer increases ε_{II}. **(G)** The suggested energy landscape at low pH, which leads to an increased energy barrier ΔG, shows a higher E_A making the transition to the unfolded state less probable, **(H)** even after applying the same trap load as in **(F)**.

30
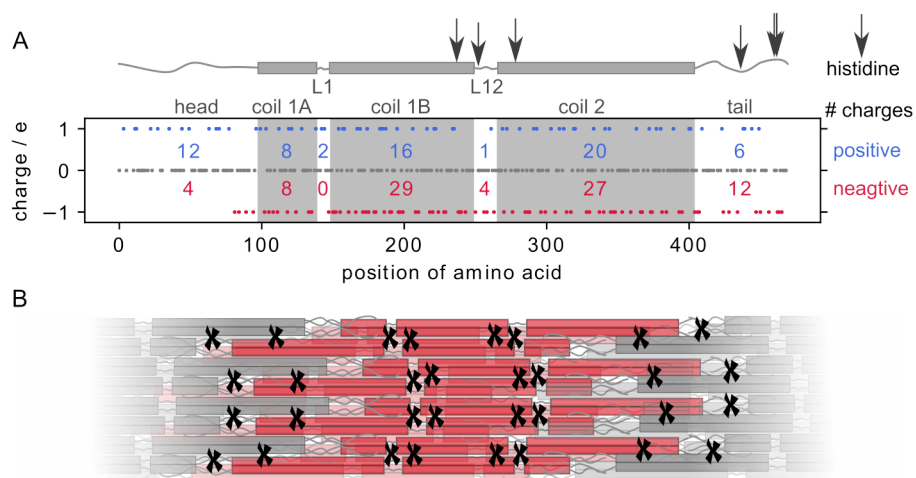
Fig. 5: Charged amino acids in vimentin. **(A)** Top: Schematic representation of the vimentin monomer. The positions of histidines in one vimentin monomer are marked with arrows. Bottom: The charges of the amino acids are plotted versus their position in the sequence. The number of amino acids that carry a positive (lysine and arginine, blue) or negative charge (aspartic acid and glutamic acid, red) at pH 7.4 are shown for the head, coils, linkers and tail. **(B)** The possible additional intra-filament interaction sites upon charge changes in the histidines are marked by 'x' for the visible front half of the red ULF.

545 **Supplementary Materials**
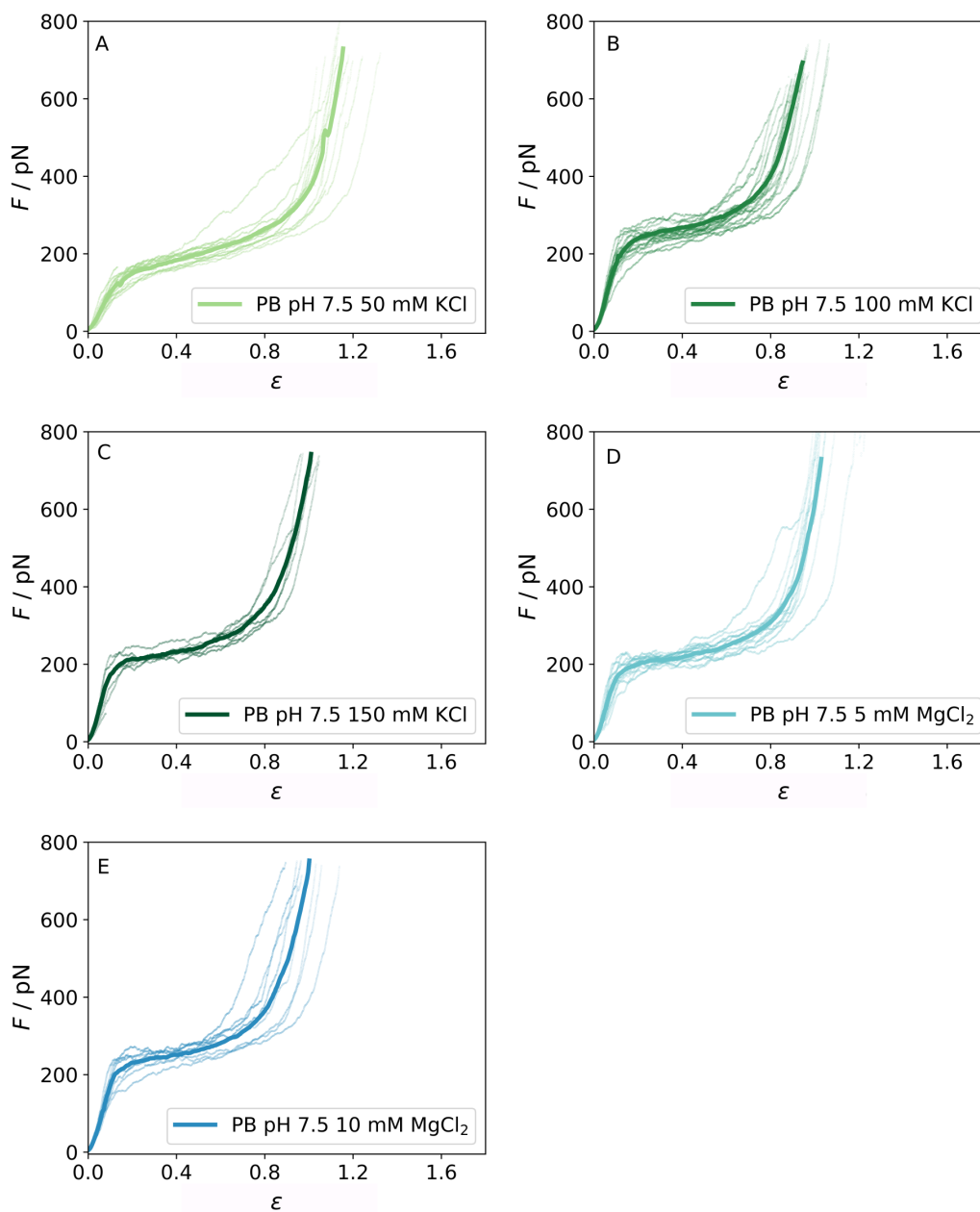
Fig. S1: Force-strain curves for each salt condition measured. (A)-(E) All single measurements of meta stable and stable filaments are plotted (thin lines) along with the average curves (bold lines, as shown in Fig. 2a in the main text).

33
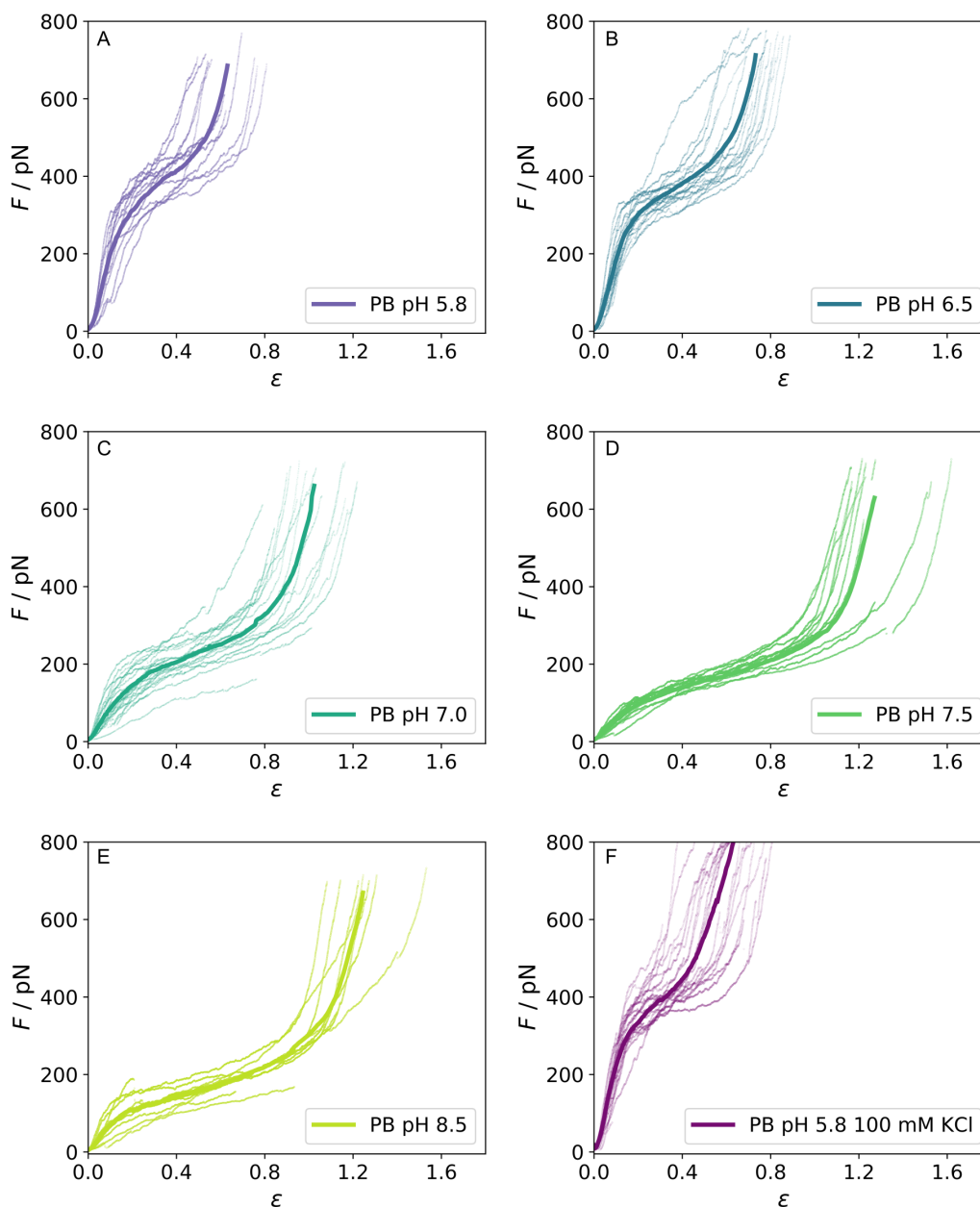
Fig. S2: Force-strain curves for each pH condition measured. All single measurements of meta stable and stable filaments are plotted (thin lines) along with the average curve (bold lines, as shown in Fig. 2b) **(A)-(E)** Show data recorded at increasing pH values and **(F)** measurements at pH 5.8 with 100 mM KCl.
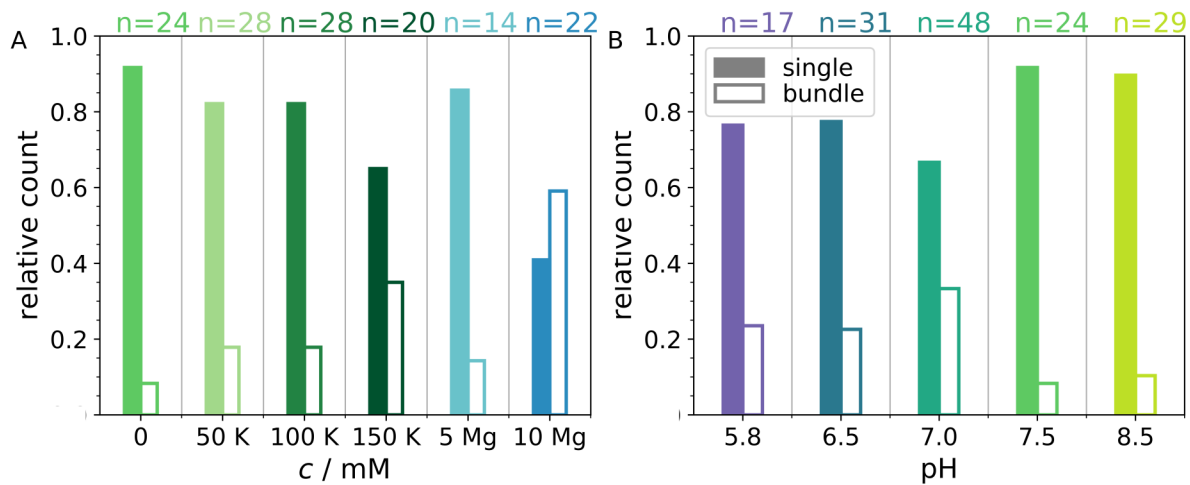
Fig. S3: Relative count of single filaments and bundles for each condition. The bundles were identified from the confocal images and from the force data. Only single filaments were used in further analysis. **(A)** The increased fraction of bundles at higher salt concentrations indicates that the ions promote filament bundling. **(B)** The fraction of bundles does not show a trend at different pH conditions.
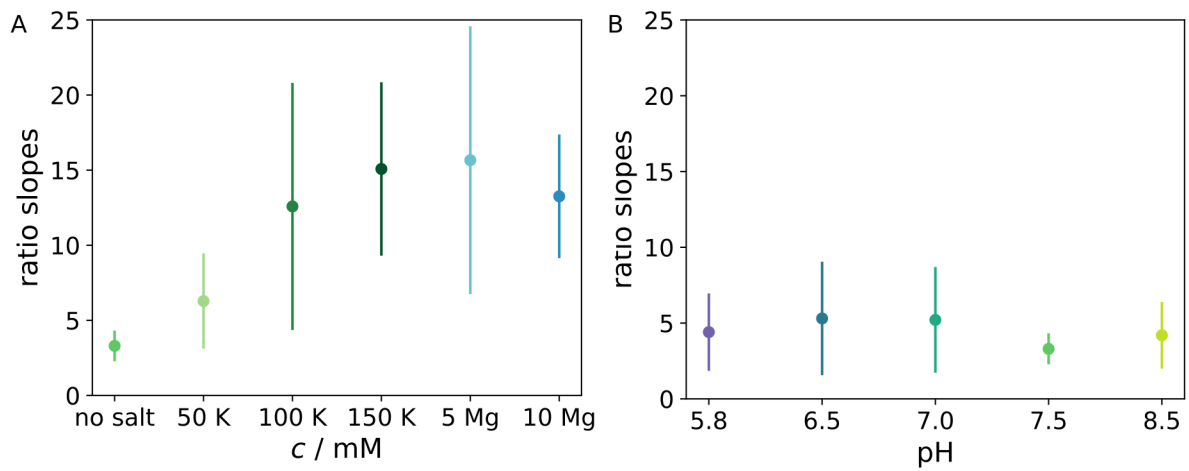
Fig. S4: The ratio of the initial slope and the slope of the plateau for each measuring condition. The respective slopes are presented in Fig. 3 in the main text. **(A)** The ratio changes at different salt conditions as the plateaus have the same slope, whereas the initial increase changes at different salt conditions. **(B)** The ratio of the slopes in buffers of increasing pH stays relatively constant.
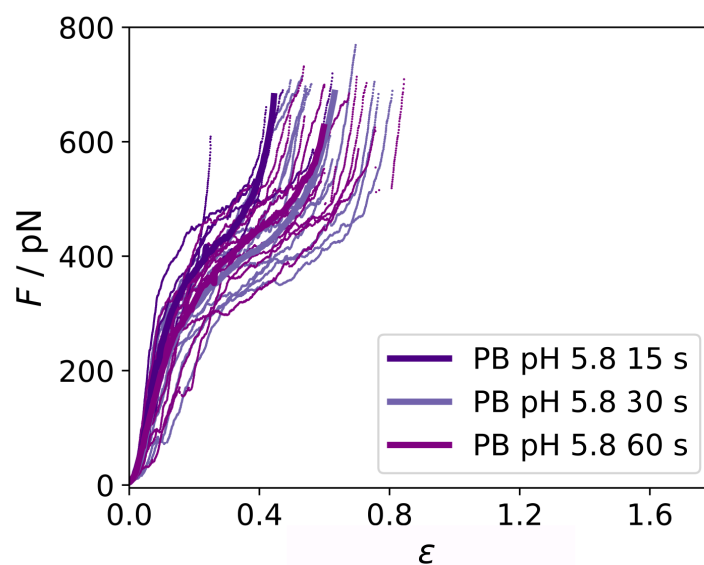
Fig. S5: Force-strain curves for filaments stretched in phosphate buffer (PB), pH 5.8 with varying incubation times. All single measurements are plotted by thin lines, the average curves are shown by bold lines. Within the variation of the single curves in each condition there is no difference apparent between the incubation times.
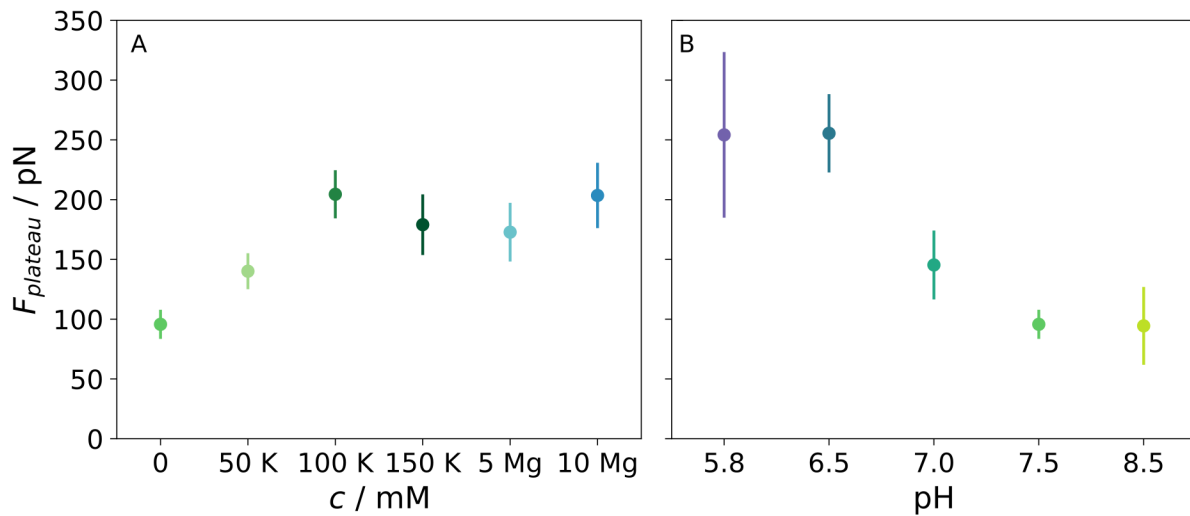
Fig. S6: Plateau force of the force-strain curves. The force at ε_I is shown for all single force-strain curves for each condition. The error bars correspond to the standard deviation. **(A)** F_{plateau} from curves recorded at pH 7.5 with varying salt concentrations. The plateau is shifted to higher forces for higher KCl concentrations or in the presence of $MgCl_2$. **(B)** F_{plateau} extracted from the force-strain curves measured at varying pH values. The plateau appears at higher forces for lower pH conditions.
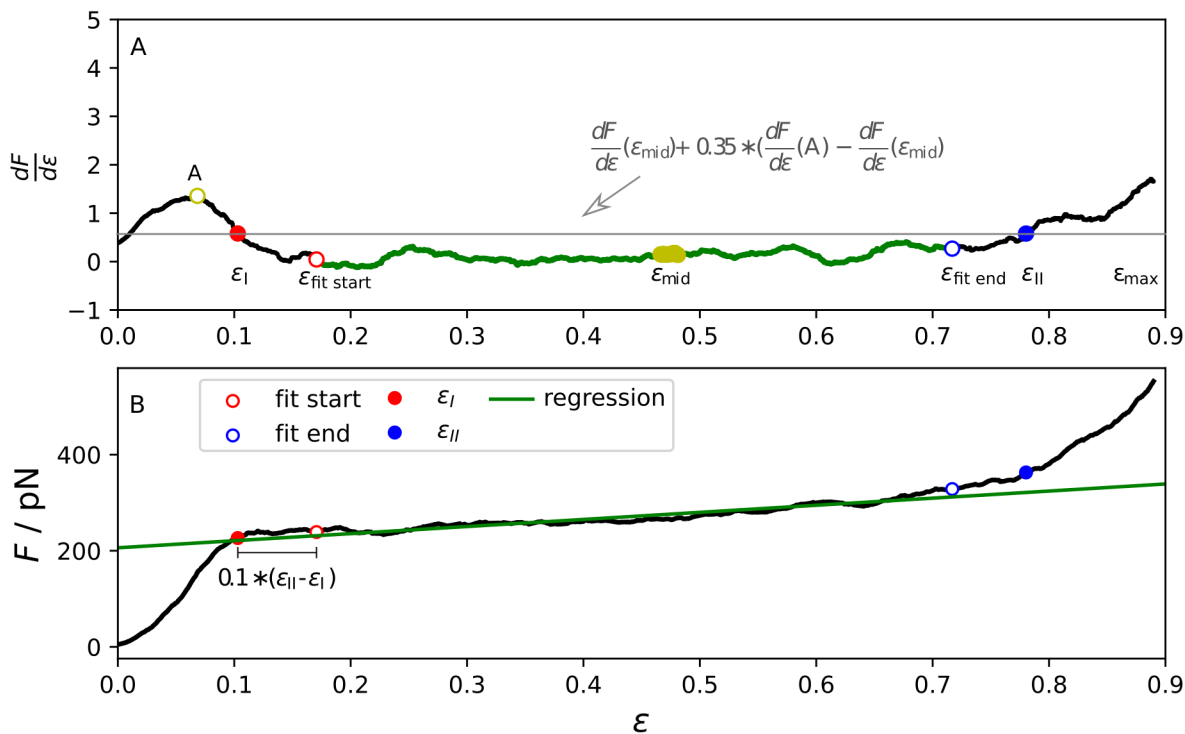
Fig. S7: Analysis of the slope of the plateau for one single force-strain curve. (A) Differential force-strain curve, smoothed with a moving average with the window width of $\frac{1}{20}$ of number of data points in the curve before $\varepsilon_{\mathrm{max}}$. The centre of the curve ($\varepsilon_{\mathrm{mid}}$) is marked in yellow. The peak of $\frac{dF}{d\varepsilon}$(A) is shown with the open yellow circle. The threshold for the plateau is indicated with the grey line. The values for ε_{I} (red, solid) and $\varepsilon_{\mathrm{II}}$ (blue, solid) at the threshold are shown. The open red and blue circles flank the region used for the calculation of the regression (green).

(B) Resulting regression plotted together with the raw force-strain curve.
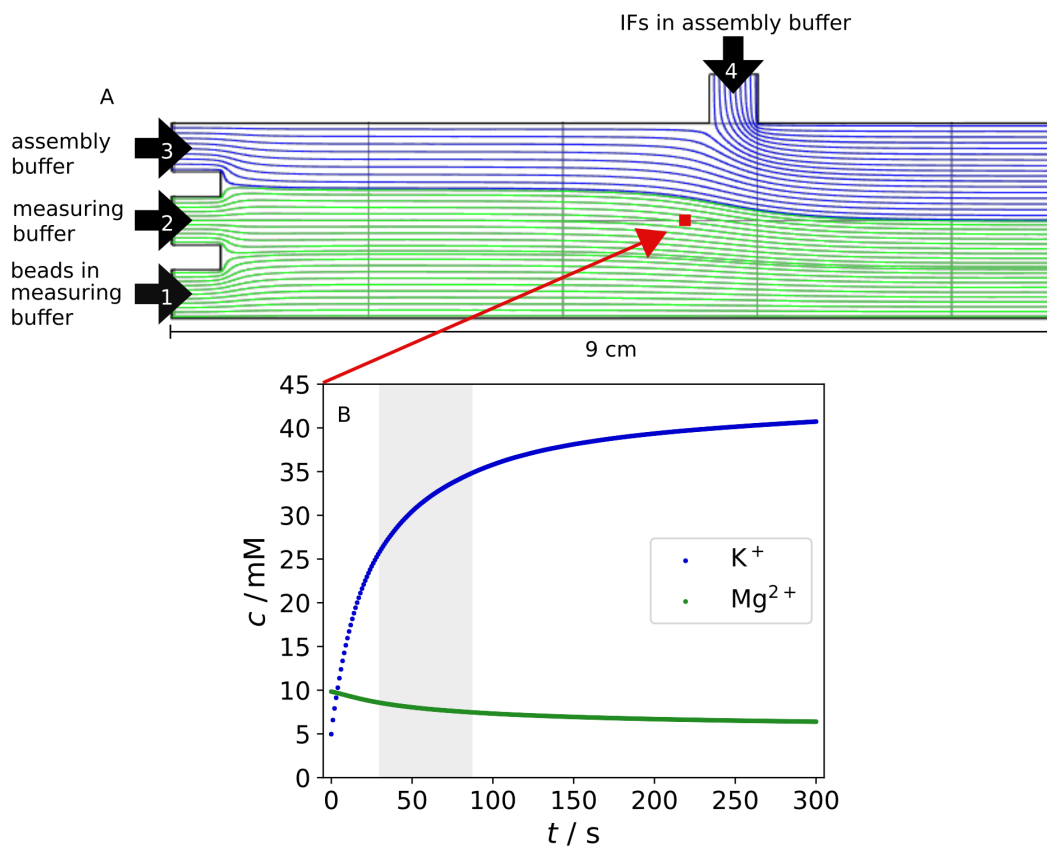
Fig. S8: Results of FEM simulations. (A) Schematic of the flow cell including simulated stream lines of the in-flowing buffers. In the experiment, beads in measuring buffer are injected in channel 1, measuring buffer in channel 2, assembly buffer in channel 3 and vimentin in assembly buffer in channel 4. The colours correspond to the cation species of the buffer (blue: K^+, green: Mg^{2+}). For this simulation, the measuring buffer contained 10 mM Mg^{2+} and the assembly buffer 100 mM K^+. IFs and beads were not included in the simulation. The position of the measurement is marked in red and corresponds to the position for which the development of the cation concentrations after stopping the flow was calculated. **(B)** Plot of the temporal evolution of the concentrations of Mg^{2+} and K^+ ions at the measurement position after stopping the flow. The time window of the measurement is indicated.